Ninth International Conference on
THIN-WALLED STRUCTURES – ICTWS2023
Sydney, Australia, Nov 29 – Dec 1, 2023

PHASE FIELD FRACTURE MODELLING FOR LASER POWDER BED FUSION METALS

Cunyi Li*, Jianguang Fang*, Grant Steven, Qing Li****

* School of Civil and Environmental Engineering, University of Technology Sydney, Sydney, NSW 2007, Australia
e-mails: Cunyi.Li@student.uts.edu.au, Jianguang.Fang@uts.edu.au

** School of Aerospace, Mechanical and Mechatronic Engineering, The University of Sydney, Sydney, NSW 2006, Australia
e-mails: grant.steven@strand7.com, qing.li@sydney.edu.au

Keywords: Phase field fracture; Transverse isotropy; Stress State, Fracture initiation; Crack propagation; Laser powder bed fusion.

Abstract. *While phase field models have been extensively studied for ductile fracture, very few have been applied to predict the additive manufactured metallic materials. This study proposes a phase field framework for modelling complex mechanical behaviour of laser powder bed fusion printed metals. To consider the fabrication induced microstructural orientation, transversely isotropic Hill48 and modified Mohr-Coulomb constitutive models are incorporated to describe the plastic and fracture behaviour, respectively. Five types of material specimens, covering a wide spectrum of stress states, are designed to identify material properties of plasticity and fracture. Three groups of crack propagation specimens are tested to demonstrate the capability of the developed model. The numerical results divulge that, by considering the stress state-dependent crack initiation, the proposed phase field model can better reproduce force-displacement responses of all specimens. Remarkably, the complex cracking sequences, including crack initiation, propagation and final rupture, can be properly captured by the proposed phase field model.*

1 INTRODUCTION

Laser Powder Bed Fusion (LPBF), a prominent additive manufacturing (AM) technology, has gained widespread adoption for diverse applications across multidisciplinary fields, including aerospace components and biomedical prostheses [1, 2]. Therefore, the characterization of mechanical behaviour in LPBF-printed materials holds paramount significance for industrial applications.

Despite the presence of extensive simulation frameworks for fracture behaviour of additive manufacturing materials, most of them rely on the use of local damage models, including the Johnson-Cook model [3], Hosford Coulomb model [4], and Modified Mohr-Coulomb models [5]. Nonetheless, local damage models [6, 7] may result in significant mesh dependency, primarily because a unique solution for strain localisation is lacking [8]. In this regard, the phase field fracture model could offer better mesh objectivity [9, 10], owing to its similarity to gradient damage models [11].

The phase field technique, which originated from the variational formulation by Francfort and Marigo [12] and was numerically implemented by Bourdin et al. [13], has gained growing popularity in the computational mechanics community attributable to its simplicity for numerical implementation. It has been utilised to replicate brittle fracture [14-16], ductile fracture [17, 18], dynamic fracture [19], and multi-field fracture [20, 21]. Up to date, only a few phase field frameworks have been conducted for additively manufactured materials in the literature. Yin et al. [22] applied an anisotropic crack surface density function incorporating

hyperelastic constitutive laws to explore the relative fracture toughness of Bouligand structures 3D-printed via the PolyJet technique. Russ et al. [23] investigated the failure mechanisms of multi-material 3D-printed polymer composites, showing that geometric parameters have a strong influence on local failure sequence and global structural resistance to fracture. To capture the mechanical resistance of interfaces of selectively laser sintered polymers, Li et al. [24] defined two damage variables accounting for two distinct fracture mechanisms at the microscale, namely bulk damage and interface damage.

This present study aims to fill the knowledge gap in phase field modelling of LPBF printed metallic materials by considering orientation-dependent plasticity and fracture. This present study aims to fill the knowledge gap in phase field modelling of LPBF printed metallic materials by considering orientation-dependent plasticity and fracture. The proposed phase field model is calibrated by material specimens and then used to predict complex crack initiation and propagation behaviour. The remainder of this paper is structured as follows. Section 2 formulates the phase field approach for additively manufactured materials. Section 3 compares the numerical results with experimental data in terms of force-displacement response, crack initiation and propagation. Section 4 concludes this work.

2 PHASE FIELD MODEL FOR LASER POWDER BED FUSION METALS

Consider an arbitrary elastoplastic body $\Omega \in \mathbb{R}^{dim}$ (where dim stands for the spatial dimension) with external boundary $\partial\Omega$ and internal discontinuity boundary Γ as illustrated in Figure 1a. Let $\partial\Omega^h$ and $\partial\Omega^s$ be the Dirichlet boundary and the Neumann boundary, respectively, satisfying $\partial\Omega^h \cap \partial\Omega^s = \emptyset$ and $\partial\Omega = \overline{\partial\Omega^h \cup \partial\Omega^s}$. In the phase field framework, the sharp interface Γ is approximated diffusely by a phase field variable d ($0 \le d \le 1$), as illustrated in Figure 1b. $d = 0$ represents that the material remains intact, while $d = 1$ indicates a completely broken crack.

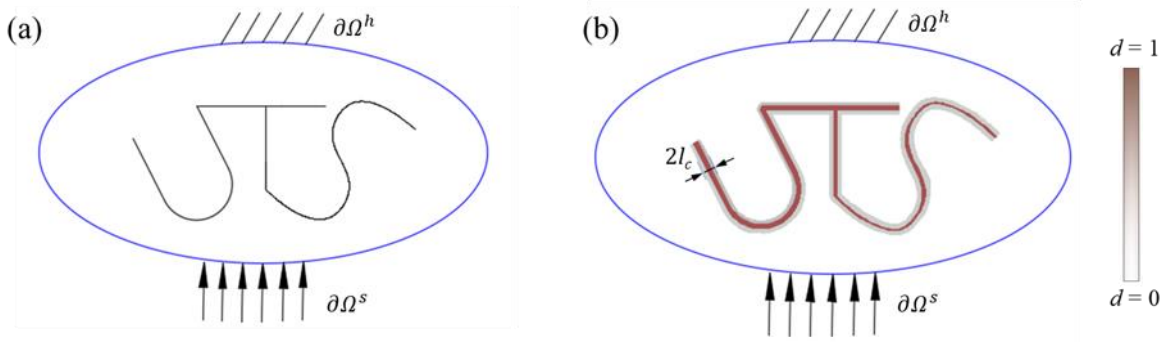

Figure 1 Crack topology of a solid with Dirichlet boundary $\partial\Omega^h$ and Neumann boundary $\partial\Omega^s$. (a) Sharp representation of interfacial discontinuity Γ; (b) Diffusive crack represented by a phase field variable d with a length scale parameter l_c to govern the crack width.

The regularised description of crack functional in multi-dimensional setting reads [16]:

$$\Theta(d) = \int_{\Omega} \frac{1}{2l_c}(l_c^2 \nabla d \cdot \nabla d + d^2)\mathrm{d}\Omega, \tag{1}$$

where $\frac{1}{2l_c}(l_c^2 \nabla d \cdot \nabla d + d^2)$ defines the cracking surface density function per unit volume of the solid. Let g_f denote the energy required to create a unit area of the fracture surface, and then the fracture energy can be obtained as [25, 26]:

$$\Xi(d) = \int_{\Gamma} g_f \mathrm{d}\Gamma \cong \int_{\Omega} \frac{g_f}{2l_c}(l_c^2 \nabla d \cdot \nabla d + d^2)\mathrm{d}\Omega. \tag{2}$$

2.1 Energy functional and governing equations

The total energy functional is formulated as follows:

$$\Pi(\mathbf{u}, \bar{\varepsilon}^p, d) = \underbrace{\int_\Omega \varphi^e(\boldsymbol{\varepsilon}^e, d)\mathrm{d}\Omega}_{\text{Elastic energy}} + \underbrace{\int_\Omega \varphi^p(\bar{\varepsilon}^p, d)\mathrm{d}\Omega}_{\text{Plastic energy}}$$
$$+ \underbrace{\int_\Omega \frac{g_f}{2l_c}(l_c^2 \nabla d \cdot \nabla d + d^2)\mathrm{d}\Omega}_{\text{Fracture energy}} - \left[\underbrace{\int_\Omega (\mathbf{f}\cdot\mathbf{u})\,\mathrm{d}\Omega + \int_{\partial\Omega^s} (\mathbf{t}\cdot\mathbf{u})\mathrm{d}\,\partial\Omega^s}_{\text{external work}}\right], \tag{3}$$

in which $\boldsymbol{\varepsilon}^e$ denotes elastic strain, $\bar{\varepsilon}^p$ represents equivalent plastic strain, φ^e and φ^p are elastic and plastic energy density, respectively. **u**, **f** and **t** are displacement field, body force, and boundary traction, respectively.

Following variational principle, the governing equations in strong form can be derived in Table 1.

Table 1: Strong form of governing equations.

Equilibrium equations	
Displacement field	
$\mathrm{div}\,\boldsymbol{\sigma} + \mathbf{f} = \mathbf{0}$ in Ω,	$(4a)$
$\mathbf{n}\cdot\boldsymbol{\sigma} = \mathbf{t}$ on $\partial\Omega^s$,	$(4b)$
$\mathbf{u} = \underline{\mathbf{u}}$ on $\partial\Omega^h$,	$(4c)$

where **n** denotes the outward normal to the boundary $\partial\Omega^s$, $\boldsymbol{\sigma}$ is damaged stress tensor, $\underline{\mathbf{u}}$ is the displacement field on $\partial\Omega^h$. For plasticity,

$$\dot{\bar{\varepsilon}}^p \geq 0, F_\mathrm{p}(\mathbf{u}, \bar{\varepsilon}^p) \leq 0, F_\mathrm{p}(\mathbf{u}, \bar{\varepsilon}^p)\dot{\bar{\varepsilon}}^p = 0 \text{ in } \Omega, \tag{5}$$

$$\mathrm{d}\boldsymbol{\varepsilon}^p = \mathrm{d}\bar{\varepsilon}^p \mathbf{a} \text{ in } \Omega, \tag{6}$$

$$F_\mathrm{p}(\mathbf{u}, \bar{\varepsilon}^p) = \tilde{f}(\tilde{\boldsymbol{\sigma}}) - \tilde{\sigma}_y(\bar{\varepsilon}^p). \tag{7}$$

$\tilde{\boldsymbol{\sigma}}$ $\tilde{f}$, and $\tilde{\sigma}_y$ are stress tensor, plastic yielding function, and flow stress in the undamaged configuration, respectively; $\mathbf{a} = \frac{\partial \tilde{f}}{\partial \tilde{\boldsymbol{\sigma}}}$ denotes the normal of the plastic yield surface. $F_\mathrm{p}(\mathbf{u}, \bar{\varepsilon}^p)$ stands for plastic yield criterion.

Phase field

$$2(1-d)\mathcal{H}(\mathbf{u}, \bar{\varepsilon}^p) + l_c^2 \Delta d - d = 0 \text{ in } \Omega \text{ and } \mathbf{n}\cdot\nabla d = 0 \text{ on } \partial\Omega^s. \tag{8}$$

where $\mathcal{H}(\mathbf{u}, \bar{\varepsilon}^p) \coloneqq \max_{\tau\in[0,T]} \mathcal{S}\big(state(\boldsymbol{u}, \bar{\varepsilon}^p)\big)$. $\mathcal{H}$ and $\mathcal{S}$ are crack driving force and crack driving state function and will be defined below.

2.2 Orientation dependent fracture initiation

The Modified Mohr-Coulomb (MMC) model was employed to capture the onset of crack for its demonstrated accuracy [27, 28]. It originated from the classical Mohr-Coulomb criterion and transforms the shear stress and normal stress representation into a mixed strain-stress representation $(\bar{\varepsilon}^f, \eta, \bar{\theta})$. The fracture strain $\bar{\varepsilon}^f$ is defined as [27]:

$$\bar{\varepsilon}^f(\eta,\bar{\theta}) = \left\{\frac{A}{c_2}\left[c_3+\frac{\sqrt{3}}{2-\sqrt{3}}(1-c_3)\left(\sec\left(\frac{\bar{\theta}\pi}{6}\right)-1\right)\right]\left[\sqrt{\frac{1+c_1^2}{3}}\cos\left(\frac{\bar{\theta}\pi}{6}\right)+c_1\left(\eta+\frac{1}{3}\sin\left(\frac{\bar{\theta}\pi}{6}\right)\right)\right]\right\}^{-\frac{1}{n}}, \tag{9}$$

where fracture strain depends on stress triaxiality η and Lode angle parameter $\bar{\theta}$. Two plastic parameters A and n and three fracture parameters c_1, c_2, c_3 need to be calibrated.

Further, in real-life practice, the loadings are commonly non-proportional where η and $\bar{\theta}$ vary during the loading history. Thus, it would be necessary to introduce a loading history dependent damage indicator D defined as [27]:

$$D(\bar{\varepsilon}^p) = \int_0^{\bar{\varepsilon}^p} \frac{\mathrm{d}\bar{\varepsilon}^p}{\bar{\varepsilon}^f(\eta,\bar{\theta})}, \tag{10}$$

where $\bar{\varepsilon}^p$ is the equivalent plastic strain. Damage initiates when $D=1$. Since the LPBF printed metallic materials exhibit orientation-dependent fracture [5]. To capture such phenomena, an anisotropic fracture model using a linear transformation of the plastic strain tensor [29] is used in this work. In a vector notation, the increment of the equivalent plastic strain in Eq. [30] can be modified as:

$$\mathrm{d}\bar{\varepsilon}^{p,ani} = \sqrt{\frac{2}{3}[\boldsymbol{\beta}\cdot(\mathrm{d}\boldsymbol{\varepsilon}^p)]^{\mathrm{T}}\cdot[\boldsymbol{\beta}\cdot(\mathrm{d}\boldsymbol{\varepsilon}^p)]}, \tag{11}$$

where $\mathrm{d}\boldsymbol{\varepsilon}^p$ is the incremental plastic strain vector and $\boldsymbol{\varepsilon}^p = [\varepsilon^p_{xx}, \varepsilon^p_{yy}, \varepsilon^p_{zz}, \sqrt{2}\varepsilon^p_{xy}, \sqrt{2}\varepsilon^p_{xz}, \sqrt{2}\varepsilon^p_{yz}]^{\mathrm{T}}$. $\boldsymbol{\beta}$ characterises the linear transformation defined as:

$$\boldsymbol{\beta} = \begin{bmatrix} 1 & 0 & 0 & 0 & 0 & 0 \\ 0 & 1 & 0 & 0 & 0 & 0 \\ 0 & 0 & \beta_{zz} & 0 & 0 & 0 \\ 0 & 0 & 0 & \beta_{xy} & 0 & 0 \\ 0 & 0 & 0 & 0 & 1 & 0 \\ 0 & 0 & 0 & 0 & 0 & 1 \end{bmatrix}, \tag{12}$$

where β_{xx} and β_{yy} are set to be 1 because ε^p_{xx} and ε^p_{yy} contribute equally and serve as the reference for ε^p_{zz}. Similarly, β_{xz} and β_{yz} are set to be 1 because ε^p_{xz} and ε^p_{yz} contribute equally and serve as the reference for ε^p_{xy}. When $\beta_{zz}=\beta_{xy}=1$, $\bar{\varepsilon}^{p,ani}$ reduces to the von Mises equivalent plastic strain. Basically, the anisotropy is introduced by distinguishing the contributions of each component of the plastic strain tensor. Suppose β_{zz} is a very large value, the MMC may be triggered even if the plastic strain in z direction is small.

Based on the above formulation, the crack driving state function is derived by introducing a energy-based threshold [28]:

$$\mathcal{S}(\mathrm{state}(\mathbf{u},\bar{\varepsilon}^p)) = \zeta\left\langle\frac{\tilde{\varphi}^e(\boldsymbol{\varepsilon}^e)+\tilde{\varphi}^p(\bar{\varepsilon}^p)}{\tilde{\varphi}_{cr}}-1\right\rangle, \tag{13}$$

where Macaulay bracket $\langle x\rangle := (x+|x|)/2$. The energy-based damage threshold $\tilde{\varphi}_{cr}$ is determined by stress state dependent fracture criteria (e.g., MMC herein):

$$\tilde{\varphi}_{cr} = \left(\tilde{\varphi}^{\mathrm{e}}(\boldsymbol{\varepsilon}^{\mathrm{e}})+\tilde{\varphi}^{\mathrm{p}}(\bar{\varepsilon}^{\mathrm{p}})\right)\big|_{D=1}. \tag{14}$$

Eq. (14) indicates that when the sum of elastic and plastic energies exceeds $\tilde{\varphi}_{cr}$, the crack driving state function becomes positive and then damage initiation occurs. Ideally, $\zeta = l_c\tilde{\varphi}_{cr}/g_f$ should also be a stress state dependent variable. However, ζ here is assumed to be a

constant material parameter for simplification [28], following the typical formulation in phase field approaches to control the damage evolution [9, 31, 32].

To better illustrate the proposed model, we present a conceptual diagram in Figure 2. Three stages exist during the loading process, namely elastic stage $\mathbb{E}$, elastoplastic stage $\mathbb{EP}$ and elastoplastic-damage stage $\mathbb{EPD}$. When the stress goes beyond the initial yield stress, the plastic deformation occurs and the damage indicator D begins to accumulate until reaching 1. Due to the LPBF process, the plastic deformation and accumulation of damage indicator D are governed by the transversely isotropic plasticity conditions at the elastoplastic stage. At the last stage, the crack propagates to full rupture, where the elastic modulus is degraded by the phase field damage.

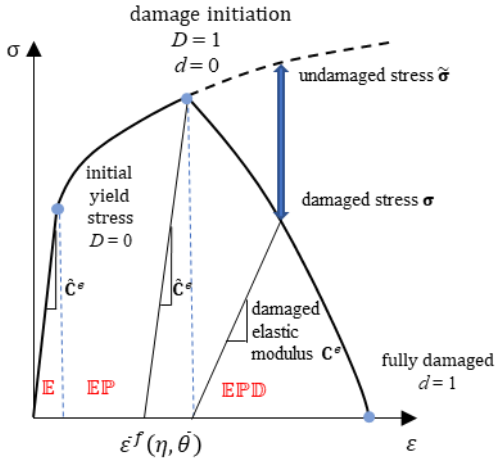

Figure 2 Conceptual diagram of the proposed phase field model for LPBF metallic materials. The response is divided into three stages, namely elastic stage $\mathbb{E}$, elastoplastic stage $\mathbb{EP}$ and elastoplastic-damage stage $\mathbb{EPD}$.

3 NUMERICAL MODELLING AND EXPERIMENTAL VALIDATION

To validate the proposed model, the modified Second Sandia Fracture Challenge [33] was used in this study. Two notches are labelled with A and D, three holes of different sizes with B, E and F, and the left edge with C, as presented in Figure 3a. Mesh discretisation with refinement in the crack propagation area was shown in Figure 3b. The numerical and experimental force-displacement curves of the modified second Sandia fracture challenge specimen are compared in Figure 4. Agreement between the numerical results and experimental data can be obtained, especially for the 0° specimen. The whole loading process is divided into seven stages as per the turning points of the simulated curves.

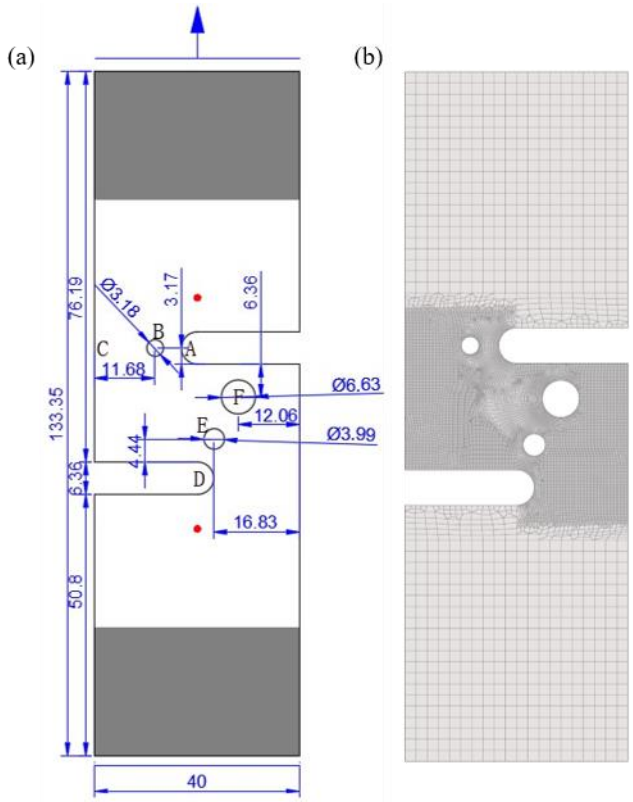

Figure 3 The modified Second Sandia Fracture Challenge. (a) Geometry and loading conditions. The two red dots indicate the points to measure the displacements. The distances of the red dots are 45 mm; (b) Mesh discretisation with the mesh size being 0.2 mm in the cracking region.

Stage I was associated with the elastoplastic deformation, where the forces increased linearly in the elastic stage and then continued increasing due to hardening for both the 0° and 90° specimens. Only minor phase-field damage from B to A could be simulated (see i of Figure 5) in this stage. The predicted global force-displacement responses and minor damage agreed with the experimental data.

In Stage II, then, a sudden drop in load was observed in both the experimental and numerical results in Stage II of Figure 4, which was due to the crack formation between A and B (ii of Figure 5). The critical displacements to fracture between A and B were 5.95 mm and 5.57 mm for both the 0° and 90° specimens, respectively, agreeing with the experimental data. It is noted that the crack was caused by tension, with a stress triaxiality of $0.4 - 0.6$ and a Lode angle parameter of $0.74 - 1.00$, in the same range of the notched tension specimens.

Stage III was further characterised by the second plastic hardening. In this stage, the damage in the left area of hole B evolved at a low rate (see iii of Figure 5). Also, the rupture between A and B was found in both the numerical and experimental results. However, the plastic hardening between B and C outweighed the fracture between A and B, leading to an increase in global force. It was found that the numerical results were consistent with the experimental data in terms of crack propagation and force-displacement response.

Stage IV was associated with the damage evolution between D and E, as shown in iii-iv of Figure 5, which resulted in the second sharp drop of the load. For the 0° specimen, the numerical force-displacement curves and predicted damage from D to E were fairly consistent with the experimental data. For the 90° specimen, the simulated damage initiation agreed with the experimental data, but damage evolution was predicted faster than the experimental

observation. This led to the discrepancy between the force-displacement curves. Specifically, in the experiment, the 90° specimen experienced a gradual and then sharp load drop, but the numerical model could only capture the sharp load drop. The material between D and E seemed more ductile in the experiment, implying that large deformation could only lead to a reduction in cross-sectional area (i.e., necking) rather than a noticeable crack.

In Stage V, the predicted damage in between D and E, as well as the left area of hole B, was further developed gradually, as shown in v of Figure 5. The combination of this slow damage evolution and plastic hardening attributed to a plateau in Stage V of the force-displacement curves in Figure 4. It is noted that the balance between hardening and damage were appropriately captured by the proposed phase field fracture model in terms of both crack development and global force-displacement responses.

Stage VI presented the third steep load drop in both the numerical and experimental curves (Figure 4) as a result of damage evolution from E to F, as shown in vi of Figure 5. The damage initiated when $u = 13.96$ mm for the 0° specimen, well matching with the experimental data. For the 90° specimen, the damage initiated when $u = 12.21$ mm, being slightly earlier than the experimental result.

Finally, in Stage VII, it is observed that the crack propagated from B to C and from E to F (Figure 5 vii). Nevertheless, the crack development was outweighed by the plastic hardening of the specimens, leading to a slight increase in the global force response (Figure 4 Stage VII). The crack near B was attributed to tensile damage, while the area near C underwent compression due to the bending deformation. Note that only tensile damage was observed, whereas compressive damage was not triggered. This was because the equivalent plastic strain induced by compression was smaller than the fracture strain, meaning that damage indicator D did not exceed 1.

To highlight the importance of fracture anisotropy in numerical modelling, we also present the results using the isotropic MMC model. For the 90° specimen, the isotropic models presented nearly the same results in terms of the force-displacement curve (in Figure 4b) and cracking path. For the 0° specimen, however, the force-displacement curve was significantly different from the experimental curve due to the inaccurate prediction of the cracking path around D (see subfigures iv-vii in Figure 5a).

In this example, we emphasise that such underestimation could result in significant errors in the prediction of crack propagation and force-displacement response. Therefore, it is essential to consider orientation-dependent fracture in numerical modelling.

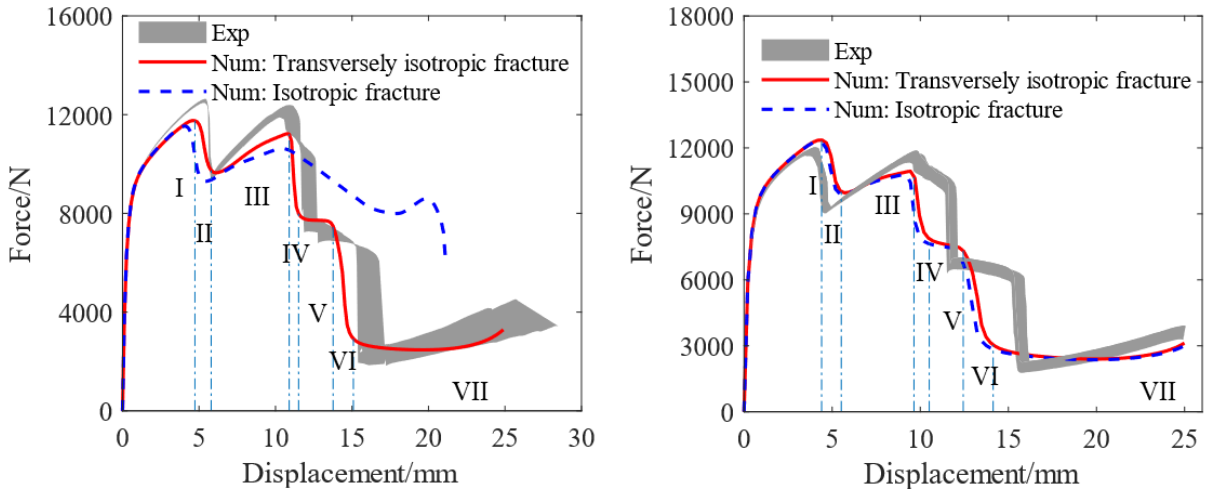

Figure 4 Comparison of the experimental and numerical results of force-displacement responses of the modified Second Sandia Fracture Challenge specimens. (a) The 0° specimens; (b) the 90°

specimens. The global response could be predicted incorrectly using the conventional isotropic model.

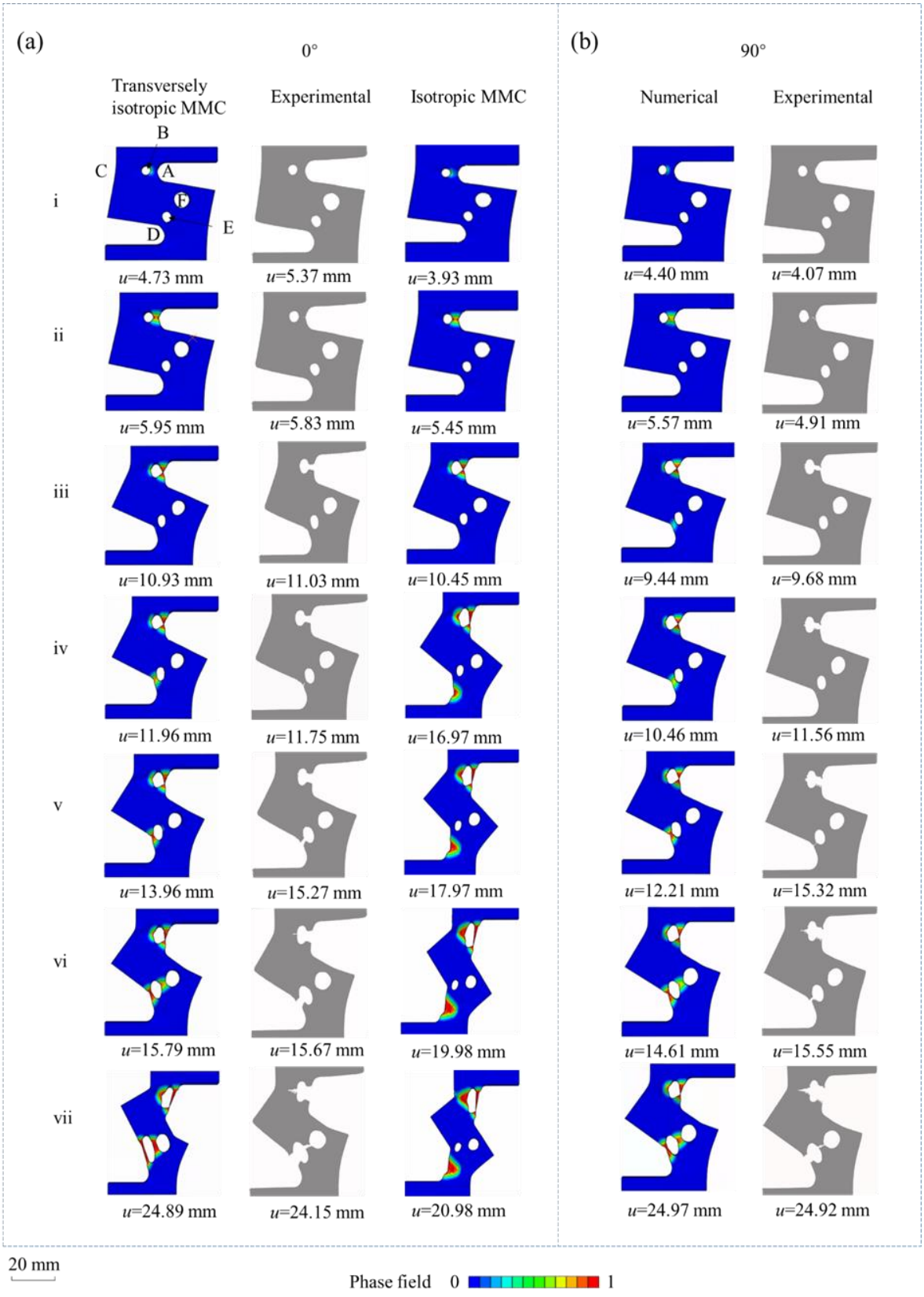

Fig. 5 Comparison of the numerical and experimental results in crack propagation of the modified Second Sandia Fracture Challenge specimens. (a) The specimens printed in the 0° orientation (left: numerical results with transversely isotropic fracture model; middle: experimental results; right: the numerical results with an isotropic fracture model); (b) The specimens printed in the 90° orientation

(Left: numerical; right: experimental). u is the displacement measured by the virtual extensometer in Fig. 3a. The key areas in specimens are labelled with letters in the first subgraph. The crack path would be predicted incorrectly using the conventional isotropic model.

4 CONCLUSION

To accurately simulate the ductile fracture behaviour of additively manufactured metallic materials, this study introduces a phase field fracture framework that accounts for material anisotropy. Elastoplastic behaviour was characterised using the Hill48 model, fracture initiation was determined by the transversely isotropic modified Mohr-Coulomb (MMC) model, and crack propagation was simulated using the phase field fracture model.

Despite the involvement of intricate crack paths in experimental samples, a notable agreement was observed between numerical and experimental results, encompassing force-displacement curves, crack initiation, and propagation. Significantly, the modification of the Second Sandia Fracture Challenge specimen underscored the critical requirement for a transversely isotropic MMC model. Utilising the conventional isotropic model would result in inaccurate predictions of the crack path, consequently leading to unacceptable discrepancies in the global force-displacement responses.

REFERENCES

[1] J. Gunasekaran, P. Sevvel, I. John Solomon, Metallic materials fabrication by selective laser melting: A review, *Materials Today: Proceedings* 37 (2021) 252-256.

[2] C.Y. Yap, C.K. Chua, Z.L. Dong, Z.H. Liu, D.Q. Zhang, L.E. Loh, S.L. Sing, Review of selective laser melting: Materials and applications, *Applied Physics Reviews* 2(4) (2015).

[3] N. Qiu, J. Zhang, C. Li, Y. Shen, J. Fang, Mechanical properties of three-dimensional functionally graded triply periodic minimum surface structures, *International Journal of Mechanical Sciences* 246 (2023).

[4] X. Li, C.C. Roth, T. Tancogne-Dejean, D. Mohr, Rate-and temperature-dependent plasticity of additively manufactured stainless steel 316L: Characterization, modeling and application to crushing of shell-lattices, *International Journal of Impact Engineering* 145 (2020) 103671.

[5] A.E. Wilson-Heid, S. Qin, A.M. Beese, Multiaxial plasticity and fracture behavior of stainless steel 316L by laser powder bed fusion: Experiments and computational modeling, *Acta Materialia* 199 (2020) 578-592.

[6] D. Mohr, S.J. Marcadet, Micromechanically-motivated phenomenological Hosford–Coulomb model for predicting ductile fracture initiation at low stress triaxialities, *International Journal of Solids and Structures* 67-68 (2015) 40-55.

[7] Y. Bao, T. Wierzbicki, On fracture locus in the equivalent strain and stress triaxiality space, International Journal of Mechanical Sciences 46(1) (2004) 81-98.

[8] G. Pijaudier‐Cabot, Z.P. Bažant, M. Tabbara, Comparison of various models for strain‐softening, *Engineering computations* (1988).

[9] C. Miehe, F. Aldakheel, A. Raina, Phase field modeling of ductile fracture at finite strains: A variational gradient-extended plasticity-damage theory, *International Journal of Plasticity* 84 (2016) 1-32.

[10] P. Areias, T. Rabczuk, M.A. Msekh, Phase-field analysis of finite-strain plates and shells including element subdivision, *Computer Methods in Applied Mechanics and Engineering* 312 (2016) 322-350.

[11] R. de Borst, C.V. Verhoosel, Gradient damage vs phase-field approaches for fracture: Similarities and differences, *Computer Methods in Applied Mechanics and Engineering* 312 (2016) 78-94.

[12] G.A. Francfort, J.J. Marigo, Revisiting brittle fracture as an energy minimization problem, *Journal of the Mechanics and Physics of Solids* 46(8) (1998) 1319-1342.

[13] B. Bourdin, G.A. Francfort, J.J. Marigo, Numerical experiments in revisited brittle fracture, Journal of the Mechanics and Physics of Solids 48(4) (2000) 797-826.

[14] G. Molnár, A. Gravouil, 2D and 3D Abaqus implementation of a robust staggered phase-field solution for modeling brittle fracture, *Finite Elements in Analysis and Design* 130 (2017) 27-38.

[15] C. Miehe, M. Hofacker, F. Welschinger, A phase field model for rate-independent crack propagation: Robust algorithmic implementation based on operator splits, *Computer Methods in Applied Mechanics and Engineering* 199(45-48) (2010) 2765-2778.

[16] C. Miehe, F. Welschinger, M. Hofacker, Thermodynamically consistent phase-field models of fracture: Variational principles and multi-field FE implementations, *International Journal for Numerical Methods in Engineering* 83(10) (2010) 1273-1311.

[17] M.J. Borden, T.J.R. Hughes, C.M. Landis, A. Anvari, I.J. Lee, A phase-field formulation for fracture in ductile materials: Finite deformation balance law derivation, plastic degradation, and stress triaxiality effects, *Computer Methods in Applied Mechanics and Engineering* 312 (2016) 130-166.

[18] J. Fang, C. Wu, T. Rabczuk, C. Wu, G. Sun, Q. Li, Phase field fracture in elasto-plastic solids: a length-scale insensitive model for quasi-brittle materials, *Computational Mechanics* 66(4) (2020) 931-961.

[19] G. Molnár, A. Gravouil, R. Seghir, J. Réthoré, An open-source Abaqus implementation of the phase-field method to study the effect of plasticity on the instantaneous fracture toughness in dynamic crack propagation, *Computer Methods in Applied Mechanics and Engineering* 365 (2020).

[20] L. Svolos, C.A. Bronkhorst, H. Waisman, Thermal-conductivity degradation across cracks in coupled thermo-mechanical systems modeled by the phase-field fracture method, *Journal of the Mechanics and Physics of Solids* 137 (2020).

[21] B. Yin, C. Steinke, M. Kaliske, Formulation and implementation of strain rate‐dependent fracture toughness in context of the phase‐field method, *International Journal for Numerical Methods in Engineering* 121(2) (2019) 233-255.

[22] S. Yin, W. Yang, J. Kwon, A. Wat, M.A. Meyers, R.O. Ritchie, Hyperelastic phase-field fracture mechanics modeling of the toughening induced by Bouligand structures in natural materials, *Journal of the Mechanics and Physics of Solids* 131 (2019) 204-220.

[23] J. Russ, V. Slesarenko, S. Rudykh, H. Waisman, Rupture of 3D-printed hyperelastic composites: Experiments and phase field fracture modeling, *Journal of the Mechanics and Physics of Solids* 140 (2020).

[24] P. Li, J. Yvonnet, C. Combescure, H. Makich, M. Nouari, Anisotropic elastoplastic phase field fracture modeling of 3D printed materials, *Computer Methods in Applied Mechanics and Engineering* 386 (2021).

[25] C. Miehe, M. Hofacker, L.M. Schänzel, F. Aldakheel, Phase field modeling of fracture in multi-physics problems. Part II. Coupled brittle-to-ductile failure criteria and crack propagation in thermo-elastic–plastic solids, *Computer Methods in Applied Mechanics and Engineering* 294 (2015) 486-522.

[26] B. Bourdin, G.A. Francfort, J.-J. Marigo, The Variational Approach to Fracture, *Journal of Elasticity* 91(1-3) (2008) 5-148.

[27] Y. Bai, T. Wierzbicki, Application of extended Mohr–Coulomb criterion to ductile fracture, *International Journal of Fracture* 161(1) (2009) 1-20.

[28] C. Li, J. Fang, C. Wu, G. Sun, G. Steven, Q. Li, Phase field fracture in elasto-plastic solids: Incorporating phenomenological failure criteria for ductile materials, *Computer Methods in Applied Mechanics and Engineering* 391 (2022) 114580.

[29] M. Luo, M. Dunand, D. Mohr, Experiments and modeling of anisotropic aluminum extrusions under multi-axial loading – Part II: Ductile fracture, *International Journal of Plasticity* 32-33 (2012) 36-58.

[30] M. Dittmann, F. Aldakheel, J. Schulte, P. Wriggers, C. Hesch, Variational phase-field formulation of non-linear ductile fracture, *Computer Methods in Applied Mechanics and Engineering* 342 (2018) 71-94.

[31] N. Noii, A. Khodadadian, J. Ulloa, F. Aldakheel, T. Wick, S. François, P. Wriggers, Bayesian inversion for unified ductile phase-field fracture, *Computational Mechanics* 68(4) (2021) 943-980.

[32] F. Aldakheel, B. Hudobivnik, A. Hussein, P. Wriggers, Phase-field modeling of brittle fracture using an efficient virtual element scheme, *Computer Methods in Applied Mechanics and Engineering* 341 (2018) 443-466.

[33] B.L. Boyce, S.L.B. Kramer, T.R. Bosiljevac, E. Corona, J.A. Moore, K. Elkhodary, C.H.M. Simha, B.W. Williams, A.R. Cerrone, A. Nonn, J.D. Hochhalter, G.F. Bomarito, J.E. Warner, B.J. Carter, D.H. Warner, A.R. Ingraffea, T. Zhang, X. Fang, J. Lua, V. Chiaruttini, M. Mazière, S. Feld-Payet, V.A. Yastrebov, J. Besson, J.L. Chaboche, J. Lian, Y. Di, B. Wu, D. Novokshanov, N. Vajragupta, P. Kucharczyk, V. Brinnel, B. Döbereiner, S. Münstermann, M.K. Neilsen, K. Dion, K.N. Karlson, J.W. Foulk, A.A. Brown, M.G. Veilleux, J.L. Bignell, S.E. Sanborn, C.A. Jones, P.D. Mattie, K. Pack, T. Wierzbicki, S.W. Chi, S.P. Lin, A. Mahdavi, J. Predan, J. Zadravec, A.J. Gross, K. Ravi-Chandar, L. Xue, The second Sandia Fracture Challenge: predictions of ductile failure under quasi-static and moderate-rate dynamic loading, *International Journal of Fracture* 198(1-2) (2016) 5-100.